CHAPTER IV

Characterization Studies of High Poisson's Ratio BMGs

Abstract

Au-Ag-Pd-Cu-Si and Pt-Cu-Ni-P are two recently developed families of high Poisson's ratio bulk metallic glass. Both possess Poisson's ratios above 0.4 which are among the highest values recorded for any BMGs. Many recent studies on BMG's plasticity have shown that high Poisson's ratio value is indeed the common requirement for ductile BMGs.

There was much anticipation that these two alloys would have very good mechanical properties, especially ductility. Indeed, these two families of alloy display improved mechanical properties over their crystalline counterparts in many aspects. However, the Pt-based alloys were the only family that exhibits exceptional ductility while the Au-based alloys only show limited ductility similar to many other metallic glasses.

This thesis chapter focuses on the key investigations conducted on the two alloys. Hopefully, the results will lead us to understand why these two high Poisson's ratio alloys behave differently.

1. Introduction

Limited plasticity at room temperature is known to be the Achilles' heel for many bulk metallic glasses (BMGs). For instance, the iron-based BMG [1] discovered by researchers at University of Virginia was not found to be a useful material for engineering applications because of its brittle nature.

There are only a limited number of BMG compositions that exhibit good ductility. Perhaps the most striking example of plasticity would be the platinum-rich glass developed by Schroers and Johnson [2] which exhibited 20% bending plasticity in thick rods – a level never previously observed in any BMGs. Chen et al. also reported ductile BMGs that displayed "extraordinary plasticity" [3]. Their high-resolution electron microscope (HREM) observation suggested that the localized shear softening was prevented by *in situ* stress-induced nanocrystallization that arrests the shear band and prevents the material from catastrophically failure from one or a few shear banding events. This mechanism could potentially be a key for developing monolithic BMGs that have both high strength and excellent ductility [3]. However, such phenomenon is not an intrinsic property of such material and has only been observed in a small handful of systems [4, 5]. The relationship between intrinsic ductility and shear softening behavior can be explained using the Cooperative Shear Model (CSM) proposed by Johnson and Samwer [6]. The model compellingly suggests possible linkage between G/B ratio (Poisson's ratio) and plasticity.

Recent study of the brittle-to-ductile transition by Lewandowski et al. [7] shows that there is a strong correlation between plasticity and elastic modulus ratio, G/B, when

G is the shear modulus and B is the bulk modulus. The value of G/B of 0.41-0.43 is found to be a maximum for a bulk metallic glass to exhibit plasticity. The relationship between G, B, and Poisson's ratio, υ, can be given as:

$$\upsilon_{Poisson} = \frac{3B - 2G}{6B + 2G} \qquad \text{[equation IV-1]}$$

For simplicity, G and B can be combined as G/B ratio and equation IV-1 could be recast as:

$$\upsilon_{Poisson} = \frac{9}{2(G/B) + 6} - 1. \qquad \text{[equation IV-2]}$$

Based on Lewandowski's finding, to achieve good plasticity in BMG, the G/B value of less than 0.41-0.43 is equivalent to the υ of more than 0.31-0.32. This concept was recently further supported by Gu and colleagues at the University of Virginia [8] who doped $Fe_{65}Mo_{14}C_{15}B_6$ bulk amorphous steel with lanthanide metals to modify the value of υ. They demonstrated that there existed a brittle-to-ductile transition in that particular Fe-based BMG system – when υ is less than 0.32, specimens tend to be brittle.

The Poisson's ratios for Au-BMGs and Pt-BMGs were found to be 0.406 and 0.43 respectively. These are among the highest values reported for BMGs. The high value of υ for Au-BMG, although not quite as high as anticipated [9], suggests excellent mechanical properties, especially good ductility. However, experimental results suggest that this is not the case.

Many detailed investigations are certainly needed to better understand these two high Poisson's ratio glasses.

2. Poisson's Ratios Study

The Poisson's ratios for Au-BMGs and Pt-BMGs were found to be 0.406 and 0.43, respectively. These are among the highest values reported for BMGs. However, the intrinsic Poisson's ratio for crystalline Au and Pt are 0.42-0.44 and 0.37-0.39 (from various sources). Table IV-1 summarizes Poisson's ratios for various forms of Au, Pt, and Pd.

Au Alloys (crystalline)		**Pt and Pd Alloys (crystalline)**	
Pure gold	0.42[A,B]	Pure Platinum	0.39[D,E], 0.396[10]
Pure gold	0.44[C]	Pure Palladium	0.39[F]
18 karat gold alloys	0.31-0.36	Pt-Ir alloy [10] (10%Ir, 20%Ir, 30%Ir)	0.378, 0.368,0.346
Au-Pd (dental)	0.33[11]	Pt-Rh alloys [10] (10%Rh, 20%Rh, 30%Rh)	0.365,0.342,0.324
Au-BMG (experimental values)		**Pt-BMG / Pd-BMG (experimental values)**	
Best glass former	0.406	$Pt_{57.5}Cu_{14.7}Ni_{5.3}P_{22.5}$	0.42[12]
OK glass former	0.417	$Pt_{57.5}Cu_{14.7}Ni_{5.3}P_{22.5}$	0.430
Cast in Liquid N_2	0.433	$Pd_{40}Ni_{10}Cu_{30}P_{20}$	0.411
Partially crystalline	0.385		

Table IV-1: Poisson's ratio values for Au, Pt, and Pd BMGs are compared with crystalline counterparts in pure and alloyed forms.

[A] According to World Gold Council (www.gold.org)

[B] According to Y.M.Savitskii, Handbook of Precious Metals

[C] According to Wikipedia (en.wikipedia.org/wiki/Gold)

[D] According to Edelmetall-taschenbuch. Degussa. (annealed condition)

[E] According to A.S.Darling, Journal of the Institute of Metals, 1966.

[F] According to Y.M.Savitskii, Handbook of Precious Metals

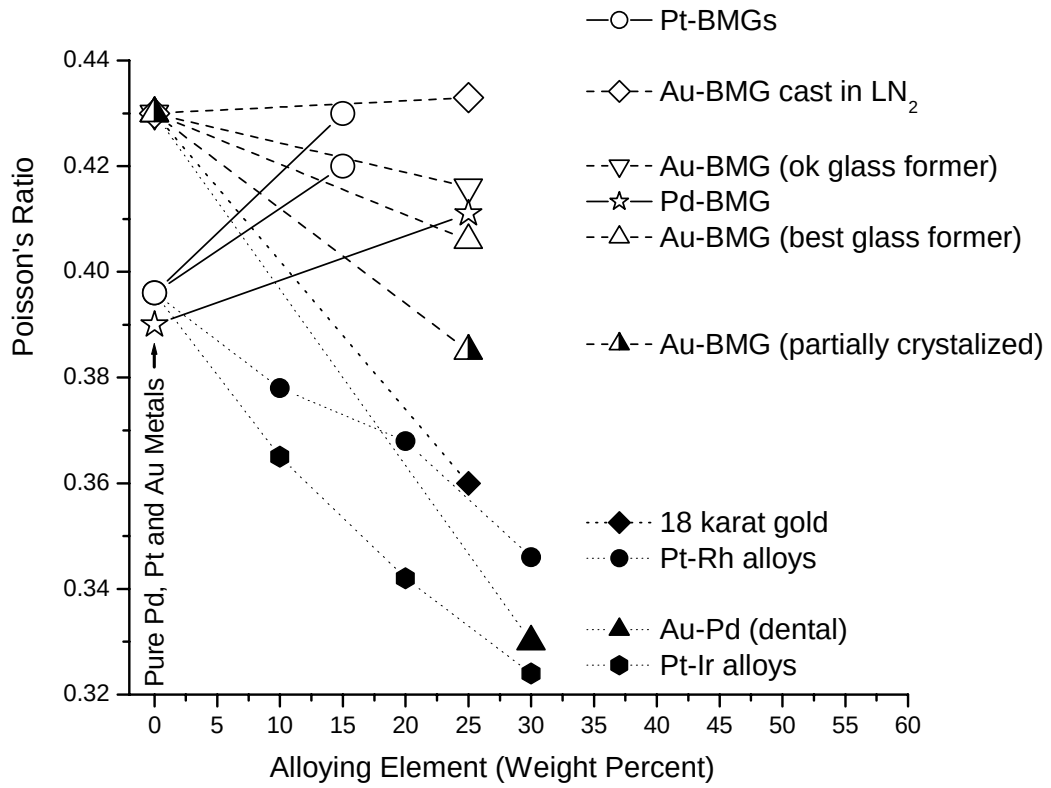

Figure IV-1: Poisson's ratios values are plotted for different alloying elements and different compositions. The open hollow symbols represent fully amorphous BMG specimens and pure elements. The solid symbols represent crystalline alloys. Half-filled triangles represent partially amorphous gold sample.

For the crystalline alloys (denoted by all "solid" symbols in Figure IV-1), the values of Poisson's ratio will decrease when the precious metals are mixed with alloying elements (e.g., Ir, Rh, Pd, Ni, Cu, etc). The rate of decrease is rather significant for Au crystalline alloys – for instance, υ drops 0.10 when Au is alloyed with Pd up to 30%. The drop in Pt Poisson's ratio is less pronounced at 0.07 drop per 30% Ir addition. In

summary, Poisson's ratio values decrease with increasing alloying element content in crystalline precious metal alloys.

The change in Poisson's ratios for bulk metallic glasses is rather curious. For Pt- and Pd-based BMGs, the υ values increase when compared to the crystalline metals in pure form. The trend is shown by solid lines linking hollow shapes in Figure IV-1. The same trend has also been observed for most BMGs (e.g. Cu-based, Zr-based, etc). This is not the case for Au-BMGs, however. Their Poisson's ratios tend to *decrease* when compared to the crystalline gold in pure form, as shown by open symbols connected by dashed lines.

It must be noted that, when the Au-BMG is cast into a liquid-nitrogen-chilled copper mold, the υ value increases, which suggests that υ value greatly depends on the processing history of the alloy. For all other Au-BMG cases studied, υ values always decrease, but not to the same extent as in their crystalline counterparts. If the υ values are compared within the Au-BMG family, the alloys with better glass forming ability show lower υ values. The alloy that is partially crystalline exhibits significant drop in υ, as shown by the half-filled triangles in Figure IV-1.

The origin of this drop in Poisson's ratios is not clearly understood. Perhaps a possible explanation could be found in the following chart (Figure IV-2). Poisson's ratio values (full table can be found in [6]) were collected only from reliable sound velocities measurement for 32 bulk metallic glasses. The υ values are subtracted by the υ values of the pure metal which is the main constituent. The differences between the Poisson's ratios, $\Delta\upsilon = \upsilon(\text{BMG}) - \upsilon(\text{pure})$, are plotted in descending order (top = largest increase and bottom = largest decrease). Our best Au-BMG displays the highest decrease in υ value.

The second highest decrease is found in the $Fe_{61}Mn_{10}Cr_4Mo_6Er_1C_{15}B_6$ BMG [13]. And the third highest decrease is the $Au_{55}Cu_{25}Si_{20}$ alloy which has critical casting thickness of 0.5 mm [14]. As demonstrated in Figure IV-2, only three BMGs at the bottom of the plot are showing negative Δυ values. All other Δυ values are positive suggesting that the υ values of BMGs tend to be higher than that of pure crystalline metals.

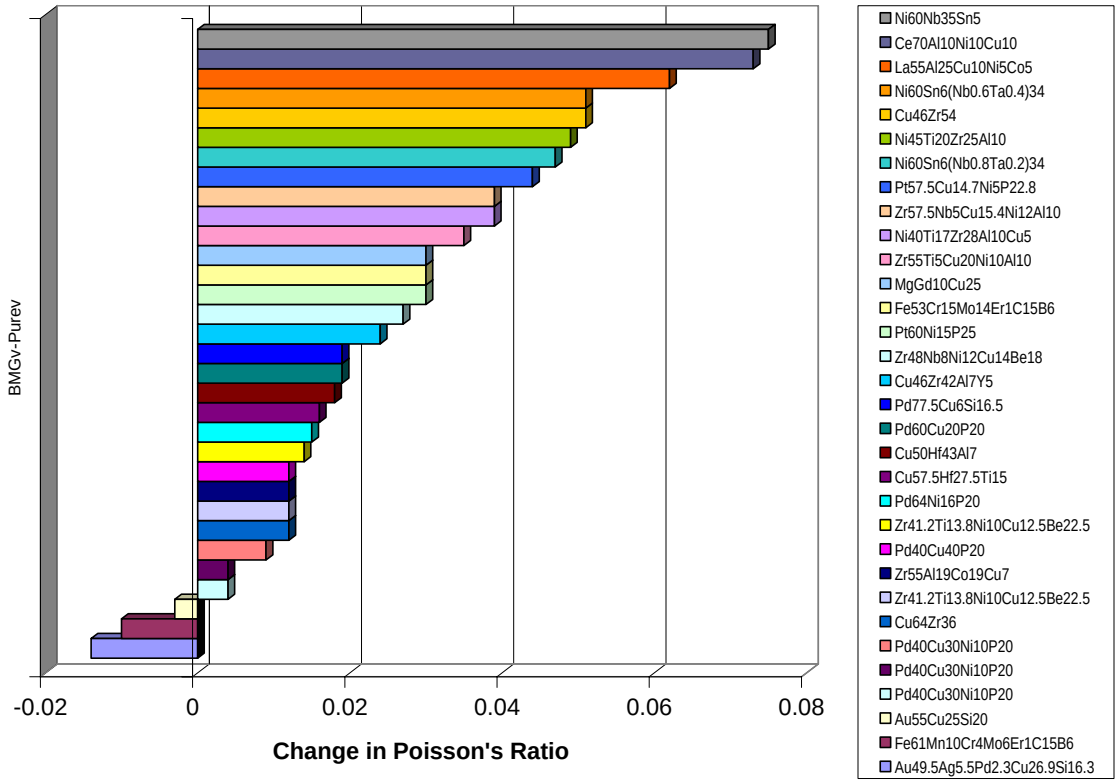

Figure IV-2: The differences between the Poisson's ratios of BMGs and pure metals are calculated using Δυ = υ(BMG)- υ(pure). Δυ for 32 BMGs are plotted in descending order (top = largest increase, bottom = largest decrease). Located at the bottom, Au-BMG exhibits the most negative change in Δυ value. Alloy index on the right is sorted in the same descending order as shown in the bar chart.

To better understand this curious υ behavior of Au-BMGs, a close investigation into $Fe_{61}Mn_{10}Cr_4Mo_6Er_1C_{15}B_6$ BMG could give a plausible explanation. The composition is the most heavily alloyed BMG to date. A total of *seven* constituents were added to form bulk glass with exceptional glass forming ability. This leads to the hypothesis that both $Au_{49}Ag_{5.5}Pd_{2.3}Cu_{26.9}Si_{16.3}$ and $Fe_{61}Mn_{10}Cr_4Mo_6Er_1C_{15}B_6$ have relatively high atomic density when compared to other BMGs. Efficient atomic packing in these super saturated BMGs could lead to increased atomic packing efficiency and decreased interatomic distances. The glass forming ability of these supersaturated alloys is improved because of the resulting increase in the fragility of the glass forming liquids when elements with strong bonding are added. The driving force for crystallization is reduced because of the sluggish atomic mobility, which is a common nature of kinetically stabilized bulk metallic forming liquids. Therefore a detailed study on density may reveal the super-saturated nature of these BMGs.

3. Density Study

To confirm the density effect of $Au_{49}Ag_{5.5}Pd_{2.3}Cu_{26.9}Si_{16.3}$ and $Fe_{61}Mn_{10}Cr_4Mo_6Er_1C_{15}B_6$ BMGS on $\Delta\upsilon$, the experimental values of the density for 25 BMGs are plotted against the calculated values based on the molar-volume calculation in Appendix A. The calculation shows accurate predicting power, as shown in Figure IV-3 where only a few P-containing BMGs were excluded. The slope of the diagonal line is unity, which represents the perfect prediction. The measured densities for both

$Au_{49}Ag_{5.5}Pd_{2.3}Cu_{26.9}Si_{16.3}$ and $Fe_{61}Mn_{10}Cr_4Mo_6Er_1C_{15}B_6$ BMGs agree well with the prediction, which may suggest the alloys do not have unusually high density.

For most BMGs, we do not see any divergence from the norm except for all the phosphorus-containing BMGs (strictly, Pt-based and Pd-based.) These values are intentionally excluded from Figure IV-3, but included in Figure IV-4 as represented by open hexagons. The calculated prediction underestimates the density of these Pt-BMGs and Pd-BMGs. We believe the deviation from the norm is the effect of high phosphorus content, and the tendency for molar volume of phosphorus to "shrink" when the nature of bonding is changing from covalent to metallic. This effect is not pronounced in alloys containing Be, Si, or other small radii elements.

The Pd-BMG is known [15] for its small Gibbs free energy difference between the undercooled liquid and the crystal ($\Delta G_{l\text{-}x}$). Such small driving force shows that Pd-BMG is a thermodynamically stable glass. Further investigations are needed for Au- and Pt-based BMGs.

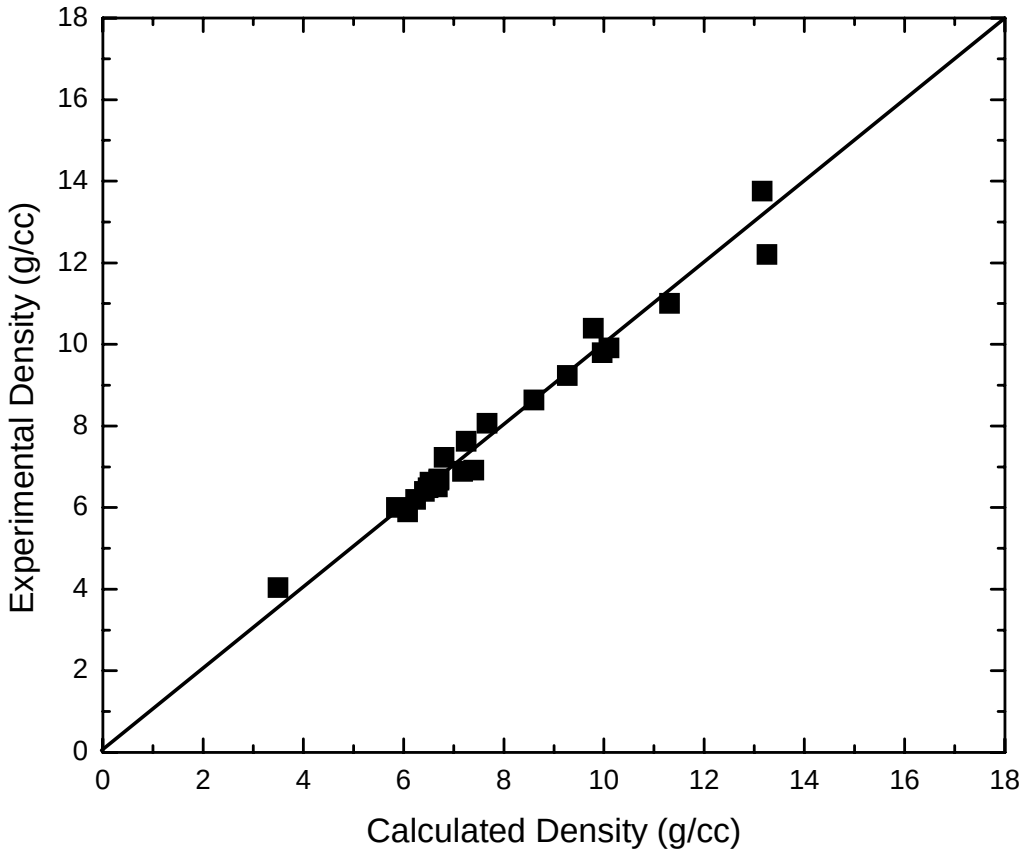

Figure IV-3: Calculated density of 25 BMGs were plotted against the experimental values. The calculation shows accurate predicting power for all alloys except the P-containing alloys, which data points are intentionally excluded. The solid diagonal line has the slope of unity (X = Y), representing an ideal prediction.

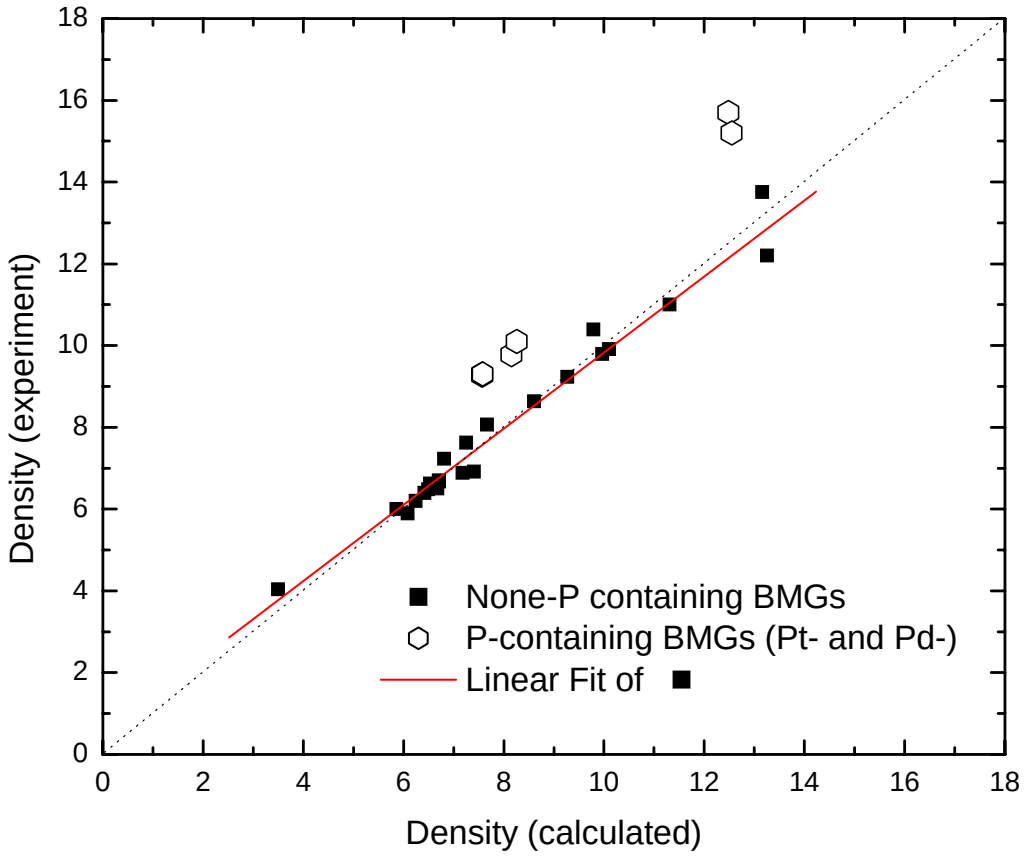

Figure IV-4: Calculated density of 31 BMGs were plotted against the experimental values. The calculation shows accurate predicting power for all alloys except the P-containing alloys, which are represented by the hexagons. The prediction always underestimates the densities of phosphorus-containing BMGs (Pt-based and Pd-based). The dotted diagonal line has the slope of unity (X = Y), representing perfect prediction. The solid trend line represents the linear fit.

4. Thermodynamic Study

4.1 Heat Capacity Measurements

We followed the experimental methods for heat capacity measurement as outlined in [16]. The absolute value of the specific heat capacity was obtained for the glassy, crystalline, and liquid state of Au-BMG ($Au_{49}Ag_{5.5}Pd_{2.3}Cu_{26.9}Si_{16.3}$) and Pt-BMG ($Pt_{57.3}Cu_{14.6}Ni_{5.3}P_{22.8}$) using a power-compensated Perkin Elmer DSC 7. Experiments were repeated systematically at small temperature increments near Tg for the glassy specimen to obtain better resolution of Cp near glass transition. The specific heat capacity measurements for both BMGs are shown in Figure IV-5. According to Kubaschewski et al. [17], the experimental data for liquid can be fitted using the relationship

$$C_{P,liquid} = 3R + aT + b/T^2, \qquad \text{(equation IV-1)}$$

where $C_{p,liquid}$ is the heat capacity of the liquid at temperature T (K), well above Debye temperature, a and b are fitting parameters, and R is the gas constant (8.314 J/g atom*K). Similarly, for the crystalline mixture, the experimental data can be fitted using the relationship [17]

$$C_{P,crystal} = 3R + cT + dT^2, \qquad \text{(equation IV-2)}$$

where $C_{p,crystal}$ is the heat capacity of the crystallized alloy (of the same composition), while c and d are fitting parameters. Experimental results are shown with the Kubaschewski fits in Figure IV-5. The solid lines represent the fitting for Au-BMG systems and dashed lines for Pt-BMG.

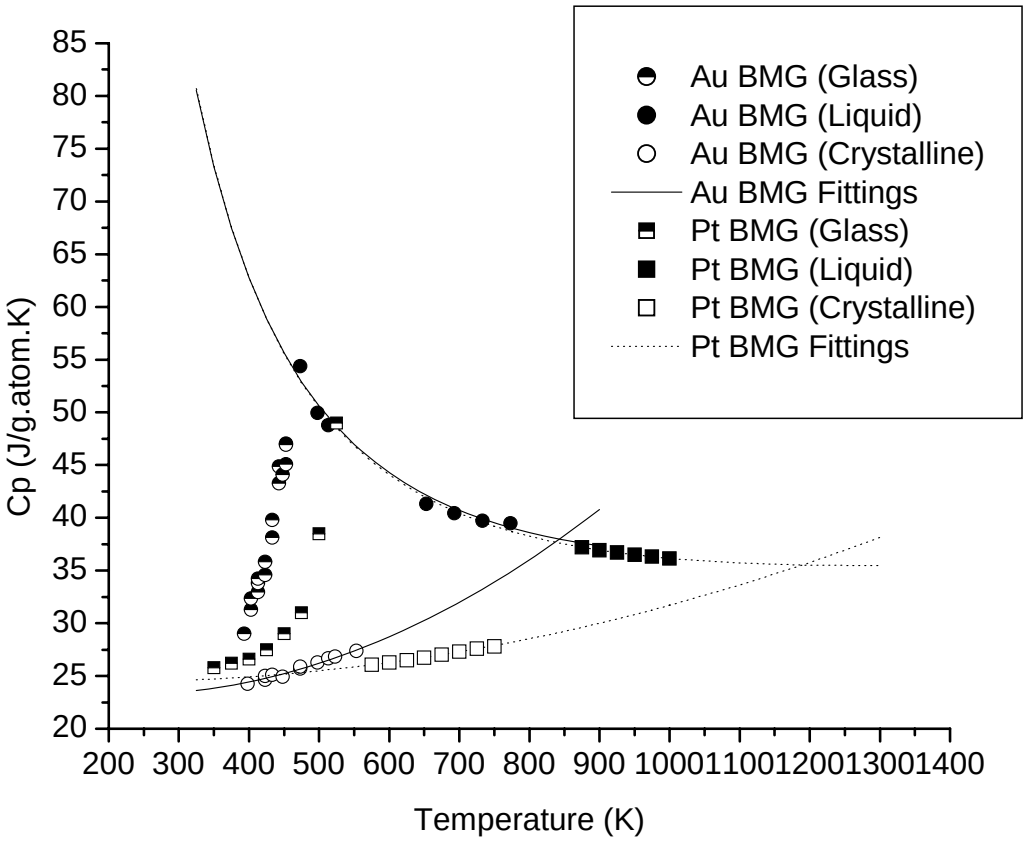

Figure IV-5: Specific heat capacities measured for $Au_{49}Ag_{5.5}Pd_{2.3}Cu_{26.9}Si_{16.3}$ (circles) and $Pt_{57.3}Cu_{14.6}Ni_{5.3}P_{22.8}$ (squares). Solid-colored shapes represent liquid, hollow, or opened shapes for crystalline, and half-filled shapes for glass.

4.2 Thermodynamic Functions Calculation

From the measured Cp data and fitted functions, it is possible to calculate various thermodynamic functions from $\Delta Cp(T)^{l-x}$. The fitting parameters for Cp as well as other experimental values are summarized in Table IV-2. The values for Au- and Pt-based alloys are fitted to the Cp values from our experiments. The Mg and Pd values are from

experiments conducted by Busch et al. [16] and Kuno et al [18]. In comparison, these values were used in the calculations for enthalpies, entropies, and Gibbs free energies.

Key Parameters	**$Au_{49}Ag_{5.5}Pd_{2.3}Cu_{26.9}Si_{16.3}$ [present work]**	**$Pt_{57.3}Cu_{14.6}Ni_{5.3}P_{22.8}$ [present work]**
a (see eq. IV-1)	5.990×10^{-3}	5.512×10^{-3}
b (see eq. IV-1)	5.676×10^{6}	5.699×10^{6}
c (see eq. IV-2)	-1.636×10^{-2}	-4.573×10^{-3}
d (see eq. IV-2)	3.776×10^{-5}	1.133×10^{-5}
Tg (K)	403 K	508 K
Tf (K)	632 K	772 K
ΔHf (J/g.atom)	6.5 kJ/g.atom	11.6 kJ/g.atom
	$Mg_{65}Cu_{25}Y_{10}$ [16]	**$Pd_{43}Cu_{27}Ni_{27}P_{20}$ [18]**
a (see eq. IV-1)	0.0137	0.012
b (see eq. IV-1)	1.8×10^{6}	4.9×10^{6}
c (see eq. IV-2)	-3.82×10^{-3}	5.4×10^{-3}
d (see eq. IV-2)	1.02×10^{-5}	1.9×10^{-5}
Tg (K)	425 K	577 K
Tf (K)	730 K	815 K
ΔHf (J/g.atom)	8.65 kJ/g.atom	5 kJ/g.atom

Table IV-2: Values of the key parameters used for Cp fittings and calculations of enthalpies, entropies, and Gibbs free energies are summarized. The values a,b,c, and d are fitting parameters. Tg, Tf, and ΔHf are experimental values.

Utilizing the fitted Cp function, the enthalpy and entropy are calculated using the following equations:

(i) $$\Delta H(T)_{l-x} = \Delta H_f - \int_T^{T_f} \Delta c_p{}^{l-x}(T')dT' \qquad \text{(equation IV-3)}$$

where ΔH_f is the heat of fusion, T_f is the fusion temperature which is generally taken as the peak temperature during melting and $\Delta Cp^{l-x}(T) = C_{p,liq} - C_{p,crystal}$ which are fitted using equation IV-1 and equation IV-2;

(ii) $$\Delta S(T)_{l-x} = \Delta S_f - \int_T^{T_f} \frac{\Delta c_p{}^{l-x}(T')}{T'}dT' \qquad \text{(equation IV-4)}$$

where ΔS_f is the entropy of fusion. The results are plotted in Figure IV-6 (ΔH) and Figure IV-7 (ΔS) accordingly.

It is known that a Gaussian distribution profile could be used to explain the $1/T^2$ dependence of specific heat. If the enthalpy is taken as the integration of the Gaussian distribution heat capacity (equation IV-3) then the enthalpy difference could be expressed [19] using the form $\Delta H = H_{infinity} - \sigma^2/T$. The basic Gaussian fits are also shown in Figure IV-6 as a comparison to the more complicated Kubaschewski model, which also contains the 1/T term.

The Gaussian fits were done using the relationship $\Delta H = H_{infinity} - k\sigma^2/T$ and the fitting parameters are:

(i) k = 8.305, σ = 751 K, and $H_{infinity}$=17243 J/g.atom for $Au_{55}Pd_{22.5}Sb_{22.5}$, and

(ii) k = 8.305, σ = 850 K, and $H_{infinity}$=15580 J/g.atom for $Au_{49}Ag_{5.5}Pd_{2.3}Cu_{26.9}Si_{16.3}$.

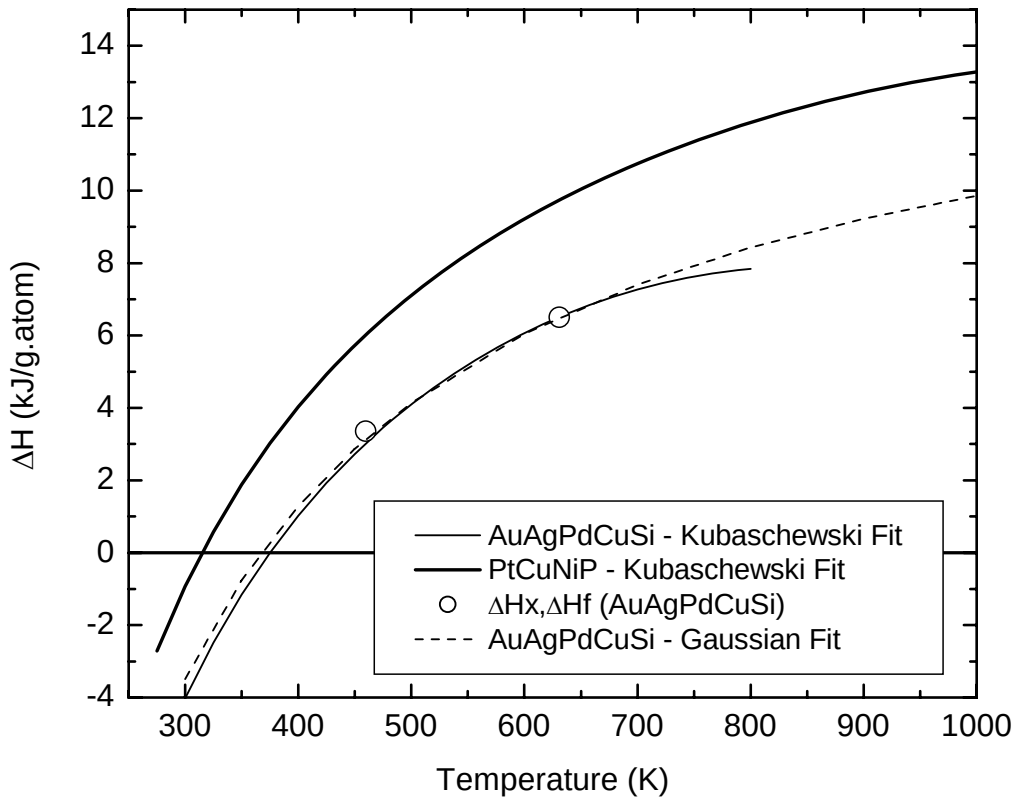

Figure IV-6: ΔH for $Au_{49}Ag_{5.5}Pd_{2.3}Cu_{26.9}Si_{16.3}$ is plotted using Kubaschewski Fit (solid thin line) and Gaussian fit [$\Delta H = H_{infinity} - \sigma^2/T$] (dashed line). ΔH for $Pt_{57.3}Cu_{14.6}Ni_{5.3}P_{22.8}$ (thick solid line) is also plotted using Kubaschewski fit.

Figure IV-6 shows the enthalpy of the undercooled liquid with respect to the crystal as a function of temperature. The horizontal line ΔH=0 represents the enthalpy of the crystal as a baseline. During cooling liquid undercools to a certain temperature and undergoes a glass transformation. The two open circles represent the Au-BMG's heat of crystallization at Tx and heat of fusion at Tf. The models predict the heat of fusion quite accurately, however the actual heat of crystallization is slightly more than the predictions.

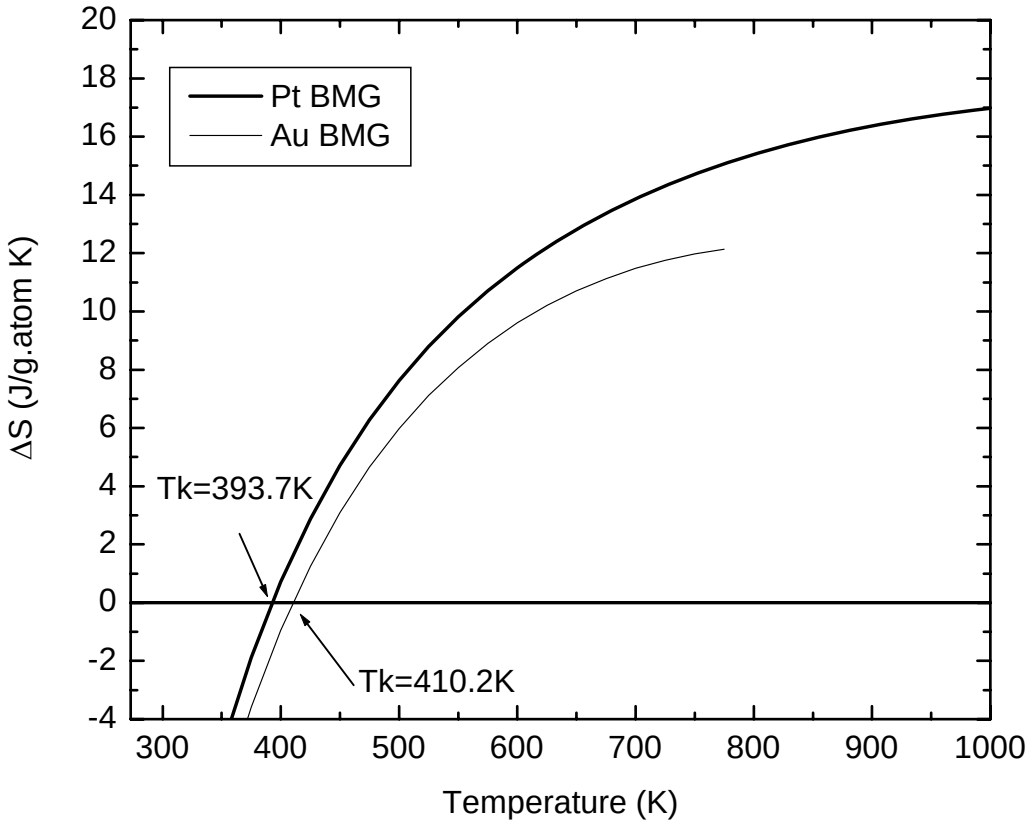

Figure IV-7: ΔS for $Au_{49}Ag_{5.5}Pd_{2.3}Cu_{26.9}Si_{16.3}$ and $Pt_{57.3}Cu_{14.6}Ni_{5.3}P_{22.8}$ are plotted. The x-intercepts correspond to the temperature where liquid and crystals have the same entropy. This temperature is known as the Kauzmann temperature, Tk. The curve indicates the improbable. Tk for Au-BMG is higher than Tg, which is around 403 K.

ΔS, the entropy differences between liquid and crystal, are plotted for both Au-based and Pt-based BMGs. The Kauzmann temperature, Tk, is the theoretical temperature at which the entropy difference vanishes. Angell and Tucker [20] suggested that an "ideal glass" could be obtained if a liquid is deeply undercooled down to a temperature near

Kauzmann temperature, Tk. Experimental results also show that all bulk metallic glasses are vitrified at temperatures Tg above Tk.

In the present work, the Kubaschewski model predicts (Figure IV-7) Platinum's Kauzmann temperature to be around 393.7 K, while the experimental Tg value is around 508 K. The difference between Tk and Tg of Pt -BMG is in line with the reported values in other BMG systems. However, the gold BMG is showing the improbable trend. Gold's Kauzmann temperature is predicted at 410.2 K while the actual value of Tg is observed at 403 K (using 20K/min heat scans). This Tg<Tk peculiarity suggests that the Kubaschewski model used for Cp fittings does not work well at low temperatures near glass transition temperature where the distribution is no longer Gaussian. An improved energy landscape model that offers a better treatment near the "wing" of the phonon distribution is required.

4.3 Generalized Sinusoidal Random Field Model

The shortcoming of the $1/T^2$-type heat capacity models (e.g., Kubaschewski model), manifests from the poor treatment of the liquid landscape in the low temperature region near Tg. Johnson et al.[19] recently proposed a potential energy landscape model based on Generalized Sinusoidal Random Fields (GSRF) which offers prudent treatment of the energy landscape near the "tail" of the distribution:

The average potential energy $\langle e \rangle = V_0 * \tanh(-W/T)$, where $-V_0$ is the energy of an ideal glass, W is the width of the logarithmic landscape and T is the temperature. At high temperatures T>W, the energy corresponds to $V_0 W/T$, which agrees with the Gaussian

distribution. The derivative of <e>, $\left.\frac{d<e>}{dT}\right|_V = Cv$, is the specific heat, which takes the form $Cv = (V_o W/T^2)\mathrm{sech}^2(W/T)$. Similarly, Cv displays the expected $1/T^2$ Gaussian dependence at high temperatures T>W.

To test the validity of the GSRF model, the ΔH for the $Au_{49}Ag_{5.5}Pd_{2.3}Cu_{26.9}Si_{16.3}$ was recalculated using only reliable data points. The experimental Cp values for both liquid and crystalline mixture (Figure IV-5) were extrapolated to only a few degrees. The experimental values of ΔCp (= $C_{p,liquid}$-$C_{p,crystal}$) were chosen from only the 550-750K temperature range because the total extrapolation of both $C_{p,liquid}$ and $C_{p,crystal}$ did not extend beyond 100 K of measured data points. The values for $C_{p,crystal}$ near Tg shall be excluded, based on our recent findings that the Kubaschewski model could not accurately describe the glass behavior near Tg.

The calculated ΔH profile based on GSRF model is shown in Figure IV-8. The GSRF model generates an enthalpy profile that tracks the 1/T trend following the Gaussian model at high temperatures. While at low temperatures (around Tg and beyond) the GSRF model shows a well-defined "tail" that eventually plateaus to a certain value (Vo).

Figure IV-9 is a version of Figure IV-8 magnified to show only the laboratory temperature range. The corresponding experimental data points agree well with the GSRF model. Open circles represent ΔH values, which were calculated directly from Kubaschewski-fitted heat capacity data points that were chosen with minimal extrapolations. The GSRF model could explain the experimental data points well over all temperature ranges. The Gaussian fit could not capture the enthalpy data point near Tg as

expected. The error bars are set at 5% for all enthalpy values, which is comparable to the 5.67% real experimental error obtained near Tg.

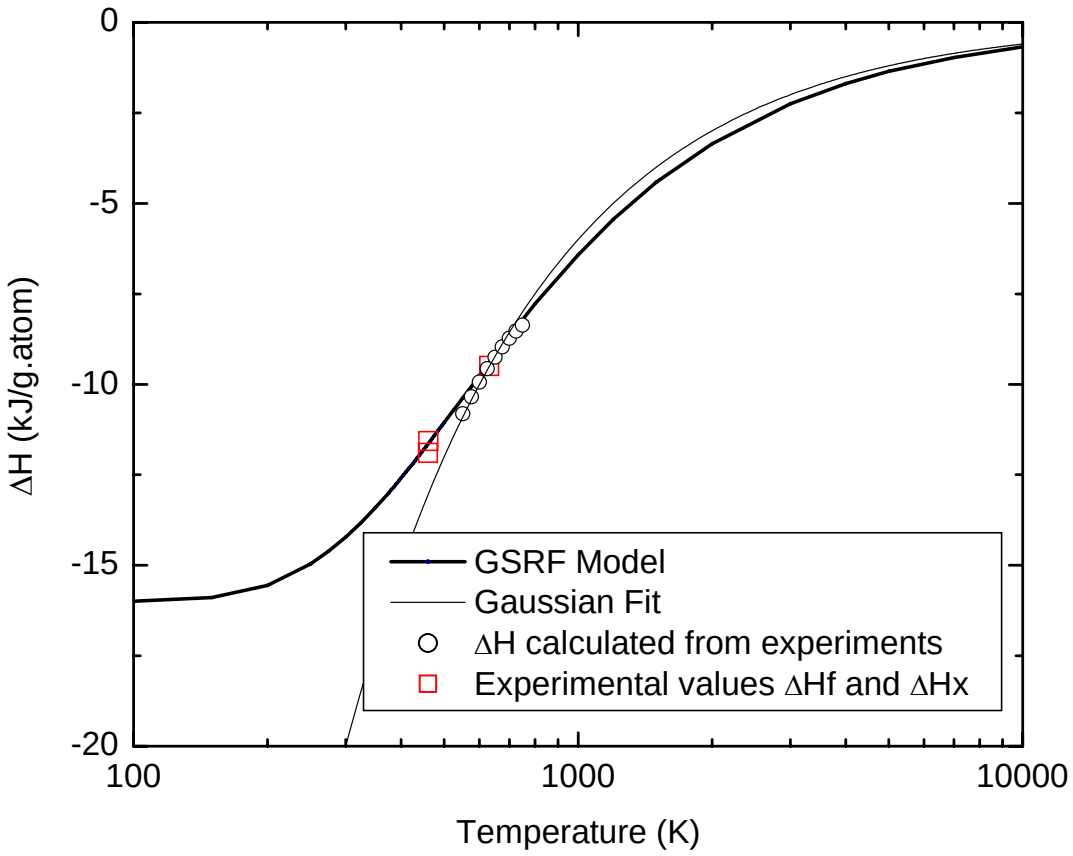

Figure IV-8: The generalized sinusoidal random field (GSRF) model offers good prediction of ΔH over all temperatures. At high temperatures (T>W) the Gaussian contribution dominates, which gives rise to the 1/T term, which also agrees well with the original Gaussian fit. At lower T, ΔH takes the logarithmic form $V_o$tanh(-W/T). The open circles represent calculated experimental results that have been extrapolated at most 100 K beyond the measured experimental values. The open boxes represent the heat of crystallization and heat of fusion measured experimentally.

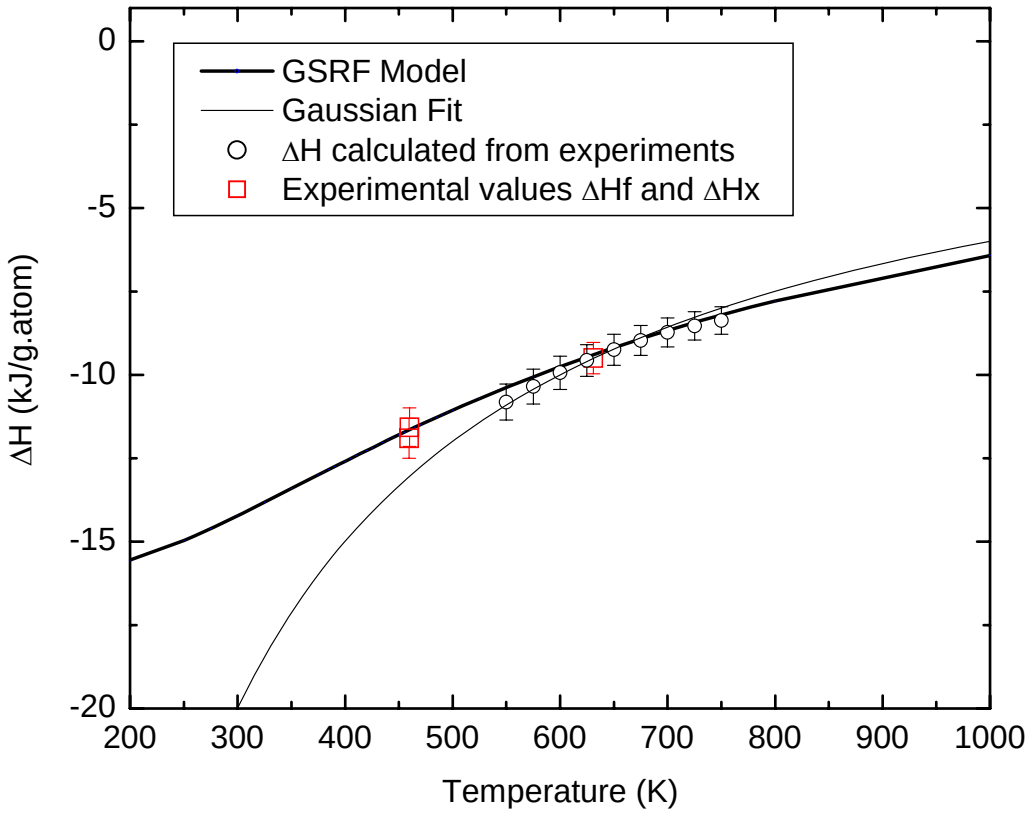

Figure IV-9: Experimental data points are selected between 550-750K, which is the temperature range where the measured experimental values are extrapolated no more than 100 K. The ability to capture the trend of ΔH during crystallization Tx up to Tf shows that the GSRF model offers a reliable mean to predict ΔH over a large temperature spectrum. Both Gaussian and Kubaschewski models only offer dependable results near Tf.

The fitting parameters for GSRF are V_o= 16000 J/g.atom (or 1924.5 K in temperature unit) and W=425 K. The value of V_o should agree with the $H_{infinity}$ fitting parameters used in Gaussian's approximation (found on page IV-15) because these two values are high-temperature energy bounds. As summarized in Table IV-3, the value of V_o is 16000 J/g.atom while $H_{infinity}$ is 15580 J/g.atom.

Moreover, V_oW can be compared to the value σ, which refers to the standard deviation of the Gaussian landscape. From GSRF, V_oW is 425x1924.5 ~ 818000 K^2 in energy unit. The value for σ^2 on the other hand is equal to 850^2 ~ 723000 K^2. All fitting parameters from the two models are in good agreement. These values are summarized in Table IV-3.

Key Parameters	**GSRF Model**	**Gaussian Model**
High temperature's maximum energy bounds	Vo = 16000 kJ/g.atom Vo = 1924.5 K	$H_{infinity}$ = 155800 kJ/g.atom
Width of the distribution	VoW = 817913	σ^2 = 722500, σ=850
Energy barrier	W = 425	W = 358 From W = σ^2/Vo

Table IV-3: Summary of key fitting parameters used in GSRF model and Gaussian model

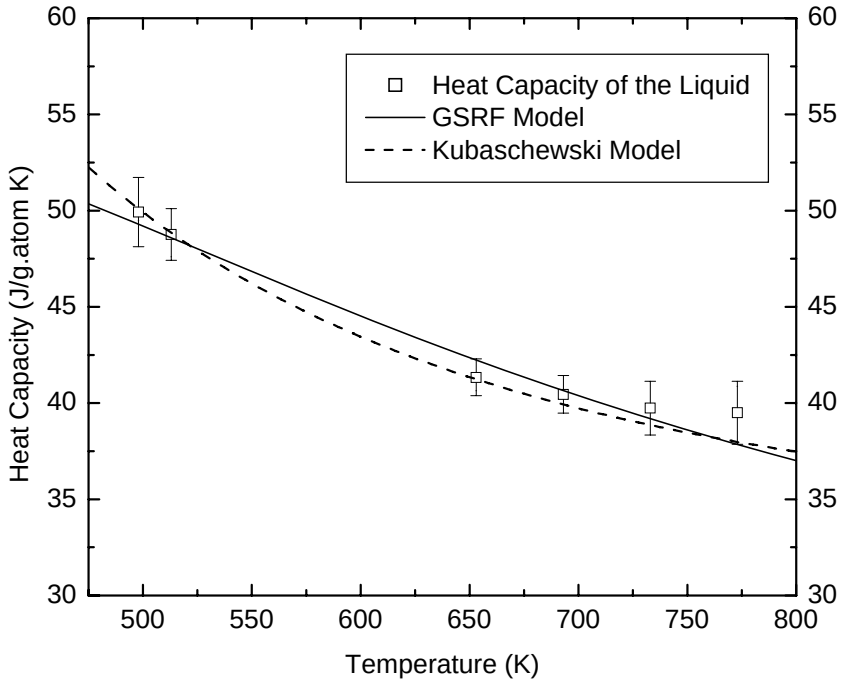

Figure IV-10: The derivative of <e>, $\left.\frac{d<e>}{dT}\right|_V = Cv$*, is the specific heat which takes the form* $Cv = (V_o W/T^2)\mathrm{sech}^2(-W/T)$*. Here, Cv calculated from the GSRF model is compared with the experimental heat capacity of the liquid (open squares) and Kubaschewski model (dash line).*

To further check the validity of the GSRF model, the heat capacity values $Cv = (V_o W/T^2)\mathrm{sech}^2(W/T)$ are plotted using the values of V_o and W which were determined in an earlier enthalpy calculation (Figure IV-9). A constant $2.5k_B$ is added to the Cv calculation as a baseline offset parameter for Cp-Cv difference ($1k_B$) and kinetic energy contribution ($1.5k_B$), which was not accounted for in the GSRF model. In Figure IV-10, the result (solid line) is shown comparing to Kubaschewski model (dashed line) and real experimental values (□).

Our final validity check is the entropy difference (ΔS) calculation. We have demonstrated that the Kubaschewski model could not accurately describe the entropy change near Tg. As a result, the Kubaschewski model predicted the Kauzmann temperature (Tk) for Au-BMG to be higher than observed glass transition temperature (Tg) (as shown earlier in Figure IV-7). As shown in Figure IV-11, ΔS values calculated using the GSRF model and Kubaschewski model are plotted with respect to time.

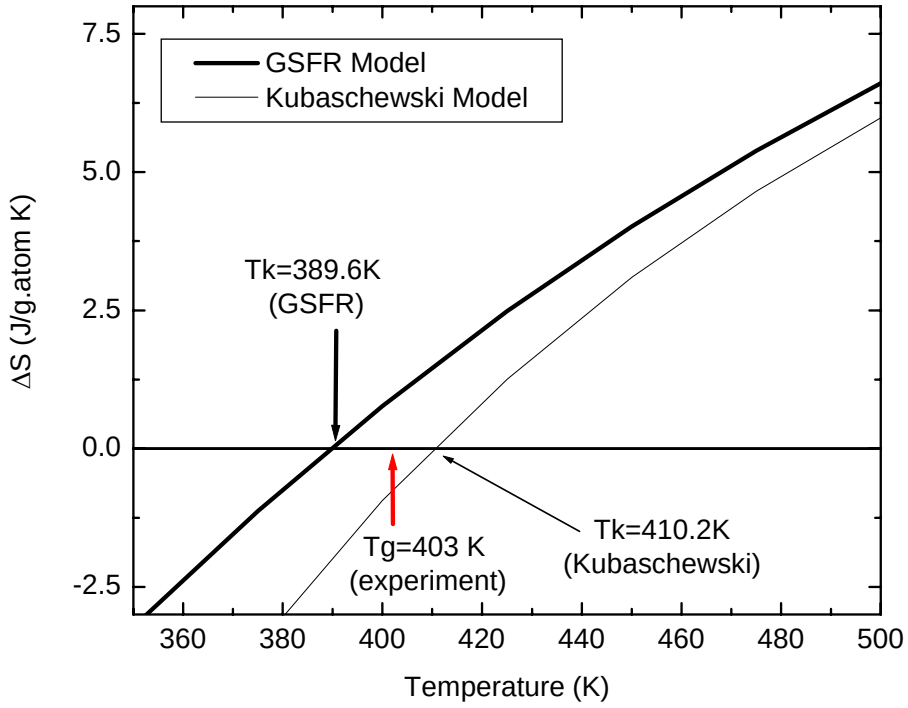

Figure IV-11: ΔS calculated using GSFR and Kubaschewski models are plotted against temperature. Both models predict different values for Kauzmann temperature, where the entropy difference between liquid and crystal vanishes. The GSFR model shows a better approximation of ΔS near glass transition, which is confirmed by the fact that the experimental value of T_g is higher than Tk.

4.4 Gibbs Free Energy Comparison

We have now demonstrated that the Kubaschewski approximation remains accurate between temperatures within 100-200 K of Tm. Many authors have been using the same thermodynamic exercise to develop the thermodynamic driving force comparison among different glass forming liquids. The difference between Gibbs free energy of liquid and crystal can readily be obtained using the thermodynamic relationship:

$$\Delta G_{l-x}(T) = \Delta H_f - \Delta S_f . T_f - \int_T^{Tf} \Delta C_P^{l-x}(T')dT' + T\int_T^{Tf} \frac{\Delta C_p^{l-x}(T')}{T'}dT' \qquad \text{(equation IV-5)}$$

where ΔH_f and ΔS_f are the enthalpy and entropy of fusion respectively, T_f is the melting temperatures, generally taken as the temperature where the maximum of the first melting peak in DSC is located [21]. ΔCp^{l-x} can be directly derived from the Kubaschewski fitting parameters of various BMGs, which can be readily found in various published articles. We have recently developed the Kubaschewski fits for both Au- and Pt-based BMGs and the following plot shows how Gibbs free energy differences in gold and platinum BMG are compared with other published alloys (Figure IV-12).

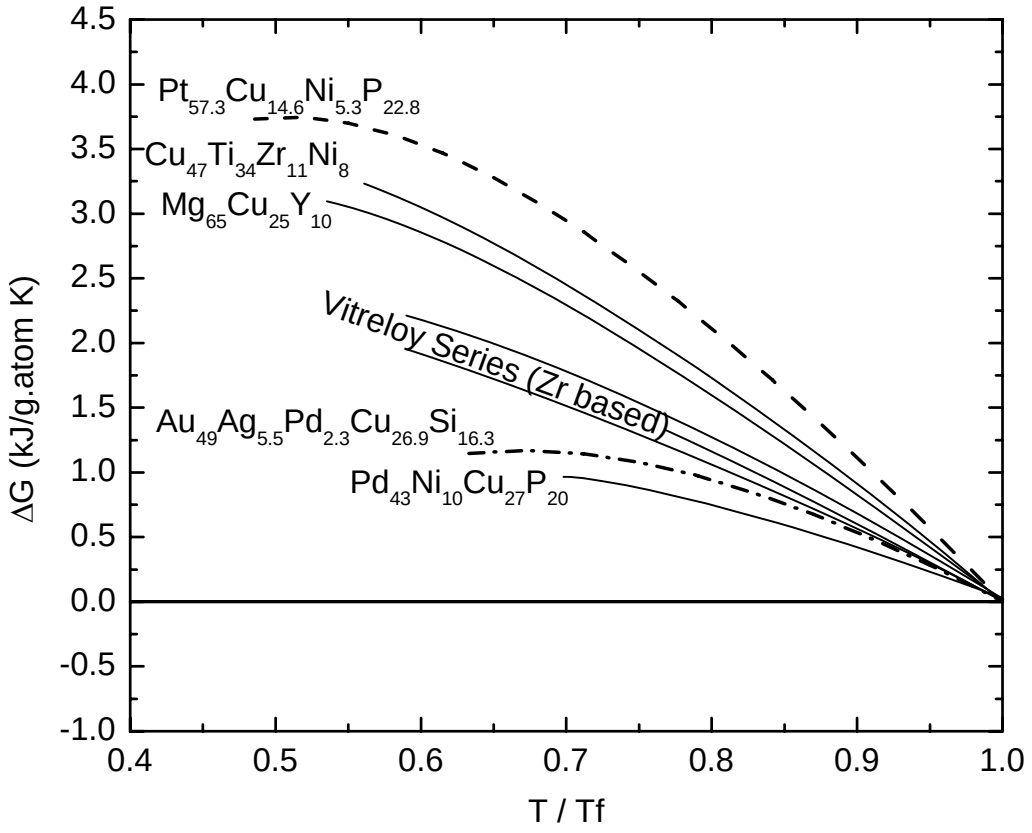

Figure IV-12: Gibbs free energy difference between the supercooled liquid and the crystalline mixture for different glass forming liquids. There is no obvious correlation between glass forming ability and ΔG projections.

Busch et al. [16] demonstrated that the Gibbs free energy difference can be used as a tool to determine the GFA of the liquids. The best glass former should have the lowest driving force for crystallization (ΔG^{l-x}) and therefore should be located at the bottom of the diagram illustrated in Figure IV-12. They found the correlation based on four metallic glass alloys. However, when the ΔG^{l-x} values for Au-BMG and Pt-BMG are compared with other bulk glass forming liquids, the trend is violated. According to Busch

et al., the ΔG curve for Pt-BMG should have been located near the Vitreloy series, and the ΔG curve for Au-BMG should have been moved up the ΔG "ladder" to near Mg-BMG because the critical casting thickness of both alloys is between 5-7 mm. Both deviations suggest that the ΔG comparison alone is not sufficient to explain glass forming ability. For example the correlation observed in Figure IV-12 is strongly affected by differences in the heat of fusion (ΔHf), which could range from 5 kJ/g.atom (Pd-Ni-Cu-P BMG) to 11.6 kJ/g.atom (Pt-Cu-Ni-P BMG).

We propose the Gibbs free energies should be compared using the free energy change framework developed by Turnbull in his seminal paper in 1969:

$$\Delta G_v = -\left\{ \Delta H_m(\Delta T_r) + T_m \int_1^{Tr} \left[\int_1^{Tr} \frac{\Delta C_p dT_r}{T_r} \right] dT_r \right\} \frac{1}{V}. \qquad \text{(equation IV-6)}$$

In equation IV-6, ΔH_m is the molar heat of fusion, T_r is the reduced temperature (T/Tm), ΔTr is (Tm-T/Tm), ΔC_p is the molar difference in heat capacity between the crystal and the liquid, and V is the molar volume of the crystal. [22] By rearranging equation IV-6 using Tr=T/Tm substitution, the expression can be simplified into two contributing terms:

$$\Delta G = -\left\{ \Delta H_m \left\langle 1 - \frac{T}{T_m} \right\rangle \right\} - \left\{ \int_{T_m}^{T/Tm} \left[\int_{T_m}^{T/Tm} \frac{\Delta C_p dT}{T} \right] dT \right\}. \qquad \text{(equation IV-7)}$$

Using equation IV-7, both contributing terms were quantitatively analyzed for all four BMGs investigated. As an example, the first and second term of equation IV-7 are plotted for comparison in Figure IV-13. The first term is represented by a line connected by open triangles, the second term by a solid line, and the resulting ΔG by a solid line connected by solid squares.

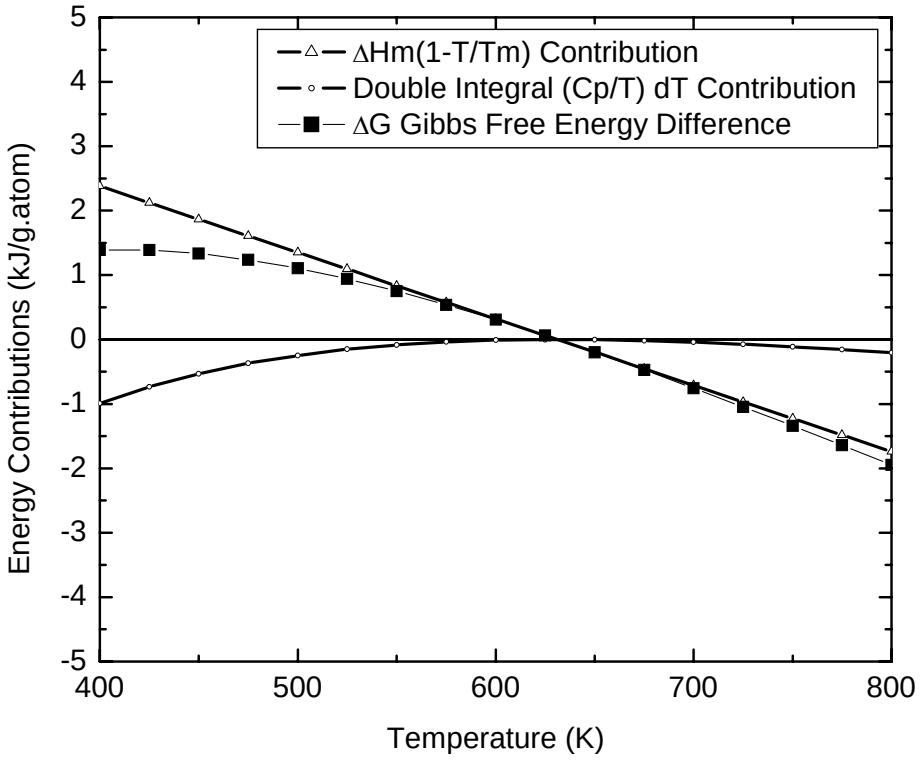

Figure IV-13: The Gibbs free energy differences are plotted using equation IV-7. Each of the two contributions is plotted separately. The double integral term is negligible near Tm which causes the ΔG values to be almost identical to ΔH_m values near Tm. This finding also suggests that the second integral term could be neglected where T is near Tm.

As illustrated in Figure IV-13, the contribution from $\int_{T}^{T/Tm}\left[\int_{T}^{T/Tm}\frac{\Delta C_p dT}{T}\right]dT$ is negligible near the melting temperatures (+/- 100 K). Therefore Gibbs free energy could be further approximated as

$$\Delta G = -\left\{\Delta H_m\left(1-\frac{T}{T_m}\right)\right\}. \qquad \text{(equation IV-8)}$$

The final result gives a simple relationship between two unit-less entities:

$$\frac{\Delta G}{\Delta H_m} = \left(\frac{T}{T_m}-1\right). \qquad \text{(equation IV-9)}$$

Equation IV-9 suggests that the normalized Gibbs free energies ($\Delta G_{l\text{-}x}/\Delta H_m$) could be used as a benchmark tool to compare the free energy differences between undercooled liquid and crystalline mixture among the different alloys. $\Delta G_{l\text{-}x}$ for all four alloys were calculated using the equation IV-5 and then plotted using the relationship shown in equation IV-9. The term "-1" in equation IV-9 will be dropped for simplicity. Figure IV-14 shows the correlation between ($\Delta G_{l\text{-}x}/\Delta H_m$), T/Tm, and d_c.

The correlation between ΔG/ΔHm and T/Tm between four vastly different alloy families appears to be universal. There is only one linear relationship, which suggests that there is only one universal ΔG/ΔHm for bulk metallic glass forming liquids. The finding is in contrast with previous findings that the difference in Gibbs free energy between liquid and crystal should be an indicator of GFA [16, 18, 23-26]. At temperatures near the melting point, our finding is in agreement with Turnbull's approximation and Richard's rule.

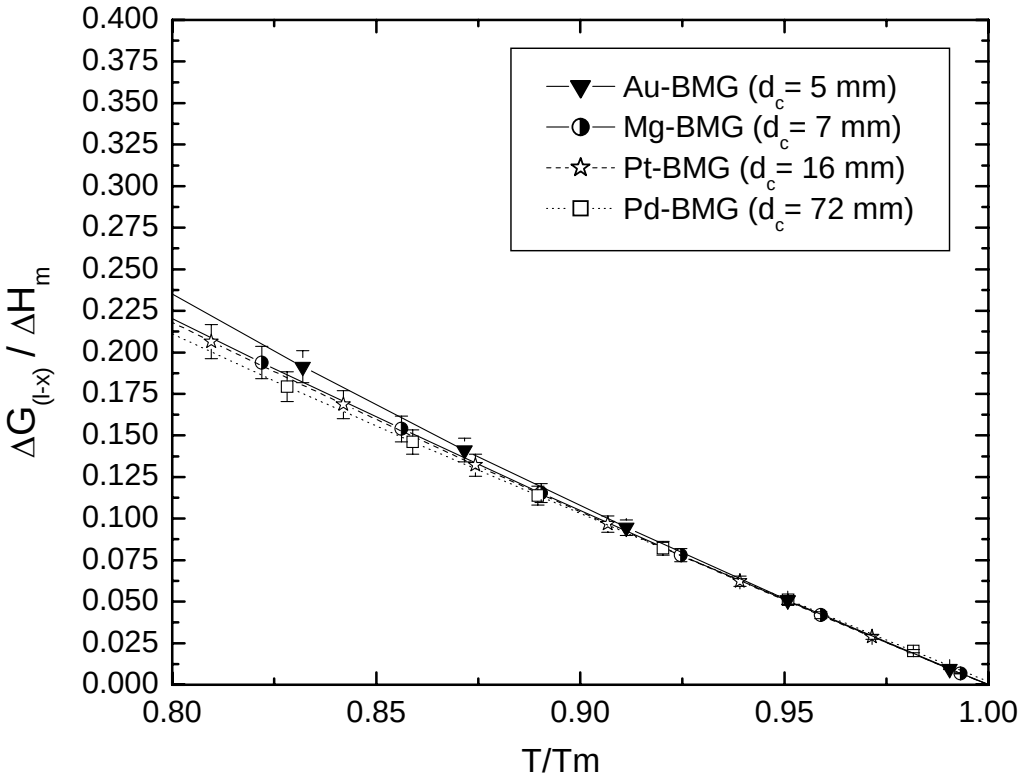

Figure IV-14: Normalized $\Delta G/\Delta H_m$ function is plotted against normalized temperature (T/T_m) to show the comparison of the Gibbs free energy difference between liquid and crystals among four bulk glass forming alloys. The dc values in parentheses indicate the maximum casting thickness of each alloy.

5. Discussions

5.1 Heat Capacity and Its Relationship to Energy Landscape

To date, one of the most acceptable and handy frameworks for interpreting and understanding glass and glass forming liquid is the energy landscape which describes the potential energy function using topology of the potential energy hypersurface. Such concept has been introduced, developed, discussed, improved, and disputed over the past 40 years[27-35]. Figure IV-15 (i) shows sections through the 3N+1 dimensional energy hypersurface of (a) strong and (b) fragile liquids where Z* represents a collective configuration coordinate[34]. As illustrated for both strong and fragile liquids, the deepest and the sharpest energy wells represent the lowest energy configuration which is crystal. All other minima (or wells) represent the mechanically stable (or meta-stable) arrangements of the particle in space or the configurational microstates which are glass. Figure IV-15 (ii), (iii) and (iv) represent respectively the level of excitation, configurational heat capacity and immediacy of Kauzmann's crisis. The configurational entropy is related to the number of minima accessible to it at a given temperature. The ΔC_p at T_g is the heat capacity increment due to gaining access to the configurational states and its value should scale with the height of the energy barriers. It is commonly found that fragile liquids have large changes in heat capacity at their T_g, implying highly degenerate landscapes[36] even quite close to T_k which is shown in Figure IV-15 (b). Angell argued that fragile liquids lack such specific bonding constraints and can therefore sample a greater variety of inherent structures[34].

The fact that our gold BMG alloy is showing the value of T_k very close to T_g and its abrupt change of ΔC_p at T_g implies that our alloy system is very fragile. During cooling, the high density of minima can be found trapped near the "ideal glass" well which is believed to be the lowest (and most stable) energy well, comparable to that of crystal. Unlike other metallic glasses, gold BMG alloy presents the opportunity to study the glassy states near "ideal glass" state which was never before possible.

The ideal glass, as shown in Figure IV-15 (i), corresponds to the lowest energy minima accessible by glassy configurons. The ideal glass state has been under heavy debates. Stillinger analytically presented that substances with molecules of bounded size interacting with physically reasonable potentials, an ideal glass transition is not possible[37]. Speedy and Debenedetti argued that this ideal state could be reached using infinitely slow densification[35, 38]. Angell and Rao believed that the ideal glass could be approached at 0 K[39] despite the fact that linear extrapolation, as shown in Figure IV-15 (ii), suggests otherwise[34].

It is important to note that as the temperature is increased, both vibrational and configurational contributions of a supercooled liquid's heat capacity should be considered. A recent study by Johari shows that vibrational parts of the heat capacity can be determined using dynamic measurement as outlined in reference [40]. He found that there is no discontinuity in the vibrational parts of C_p on structural unfreezing in the Tg range and the change in C_p at Tg is entire due to change in the configurational parts[40]. In fact, the change in the vibrational parts of C_p and thermal expansivity (α) at Tg is both negligible, and the anharmonic contribution to α of glass and liquid is almost the same.

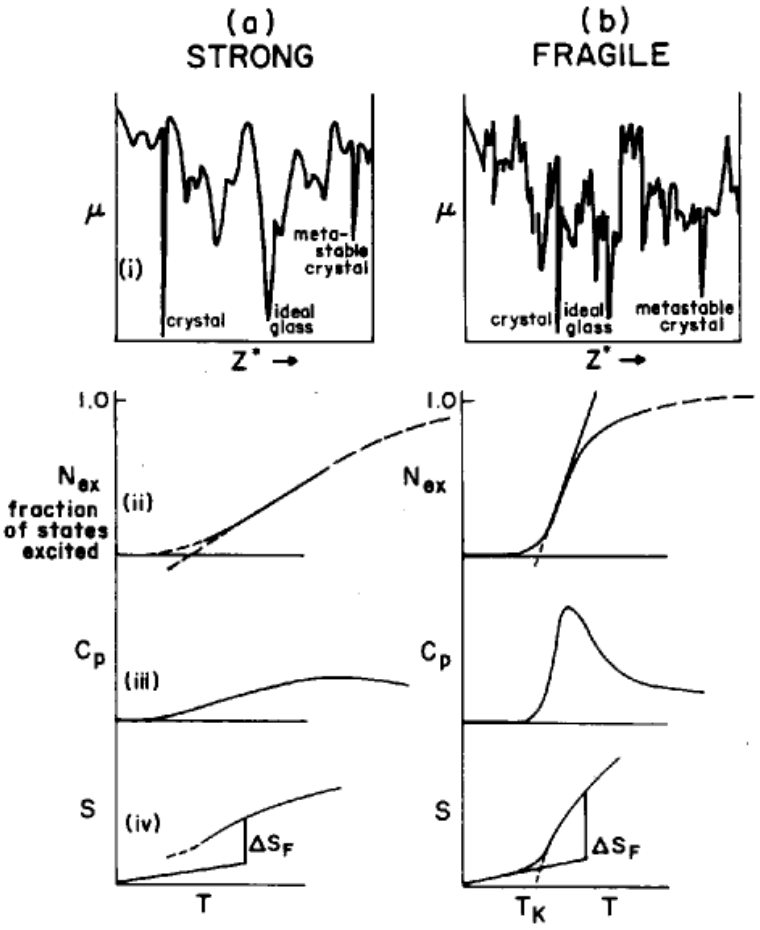

Figure IV-15: Sections through the 3N+1 dimensional energy hypersurface(i) of a strong (a) and fragile (b) liquids. Z is configuration coordinate. (ii),(iii), and (iv) show level of excitation, configurational heat capacity, and immediacy of Kauzmann entropy crisis. (Reproduced after [36] and [34])*

6. Summary

Poisson's ratio values in BMGs tend to be higher than that of their crystalline counterparts. There are only three BMGs in two alloy families that behave differently and show drop in Poisson's ratios in amorphous state. The common feature of these two systems may be that they are kinetically stabilized glasses. The GFA of these alloys is the direct result of increased Tg, which is accomplished by adding solute elements with a strong bonding nature into the melt. In particular, the Fe-BMG has seven constituents and the alloy is super-saturated with solutes. For the Au-BMG, Cu is added into alloy to primarily raise Tg from 40 ºC to 130 ºC while the liquidus temperature only changed from 363 ºC to 381 ºC.

Both Fe-BMG and Au-BMG show the expected density values as calculated using molar volume-weighted average. Topologically, Au-BMG in particular is similar to that of Pt-BMG when atomic radii of each constituent are compared.

Plasticity in BMGs may be related to the value of Poisson's ratio. However, there is no universal value that determines the brittle-to-ductile transition for all BMG systems. Poisson's ratios vary significantly with alloy systems and the correlation of Poisson's ratios to plasticity can only be applied within the same alloy family.

The Kubaschewski model for fitting Cp values is good for thermodynamic approximation near T_f. The model could not describe the behavior of Au-BMG near glass transition temperature. Generalized Sinusoidal Random Field theory offers better thermodynamic correlation over all temperature ranges.

The Gibbs free energy difference may not be the key to determining GFA of bulk glass forming alloys. The value of the $\Delta G/\Delta H_m$ ratio is universal for all liquids near Tm, which suggests that all metallic glass forming liquids may be the same thermodynamically near Tm. We have also found that the difference in Gibbs free energy alone could not explain the difference in GFA in different alloys. Most careful analysis is needed to fully understand the thermodynamic functions and their roles in determining glass forming ability.

References

[1] V. Ponnambalam, S. J. Poon, G. J. Shiflet, V. M. Keppens, R. Taylor, G. Petculescu, Applied Physics Letters 83 (2003) 1131-1133.

[2] J. Schroers, W. L. Johnson, Physical Review Letters 93 (2004) -.

[3] M. Chen, A. Inoue, W. Zhang, T. Sakurai, Physical Review Letters 96 (2006) -.

[4] A. Inoue, T. Zhang, M. W. Chen, T. Sakurai, J. Saida, M. Matsushita, Applied Physics Letters 76 (2000) 967-969.

[5] A. Inoue, T. Zhang, M. W. Chen, T. Sakurai, Materials Transactions Jim 40 (1999) 1382-1389.

[6] W. L. Johnson, K. Samwer, Physical Review Letters 95 (2005) -.

[7] J. J. Lewandowski, W. H. Wang, A. L. Greer, Philosophical Magazine Letters 85 (2005) 77-87.

[8] X. J. Gu, A. G. McDermott, S. J. Poon, G. J. Shiflet, Applied Physics Letters 88 (2006) -.

[9] W. L. Johnson, Private Communication, in: Pasadena, CA, 2005.

[10] J. Merker, D. Lupton, M. Topfer, H. Knake, Platinum Metals Rev. 45 (2001) 74-82.

[11] K. J. Anusavice, B. Hojjatie, P. H. Dehoff, Journal of Dental Research 65 (1986) 1173-1178.

[12] J. Schroers, W. L. Johnson, Physical Review Letters 93 (2004) 255506.

[13] V. Ponnambalam, S. J. Poon, G. J. Shiflet, Journal of Materials Research 19 (2004) 3046-3052.

[14] J. Schroers, B. Lohwongwatana, W. L. Johnson, A. Peker, Applied Physics Letters 87 (2005) 061912.

[15] J. Schroers, W. L. Johnson, R. Busch, Applied Physics Letters 77 (2000) 1158-1160.

[16] R. Busch, W. Liu, W. L. Johnson, Journal of Applied Physics 83 (1998) 4134-4141.

[17] O. Kubaschewski, C. B. Alcock, P. J. Spencer, O. Kubaschewski, Materials thermochemistry, Pergamon Press, Oxford ; New York, 1993, p. xii, 363 p.

[18] M. Kuno, L. Shadowspeaker, J. Schroers, R. Busch, Thermodynamics of Pd43Ni10Cu27P20 Bulk Metallic Glass Forming Alloy, in: 2005.

[19] W. L. Johnson, Potential Energy Landscape of Metallic Glasses and Liquids (to be published), in: 2007.

[20] C. A. Angell, J. C. Tucker, Journal of Physical Chemistry 78 (1974) 278-281.

[21] R. Busch, Y. J. Kim, W. L. Johnson, Journal of Applied Physics 77 (1995) 4039-4043.

[22] D. Turnbull, Contemporary Physics 10 (1969) 473.

[23] S. C. Glade, R. Busch, D. S. Lee, W. L. Johnson, R. K. Wunderlich, H. J. Fecht, Journal of Applied Physics 87 (2000) 7242-7248.

[24] R. Busch, E. Bakke, W. L. Johnson, Acta Materialia 46 (1998) 4725-4732.

[25] E. Bakke, R. Busch, W. L. Johnson, Metastable, Mechanically Alloyed and Nanocrystalline Materials, Pts 1 and 2 225 (1996) 95-100.

[26] W. N. Myung, L. Battezzati, M. Baricco, K. Aoki, A. Inoue, T. Masumoto, Materials Science and Engineering a-Structural Materials Properties Microstructure and Processing 179 (1994) 371-375.

[27] G. Adam, J. H. Gibbs, Journal of Chemical Physics 43 (1965) 139-&.

[28] Goldstei.M, Journal of Chemical Physics 51 (1969) 3728.

[29] M. Goldstein, Journal of Chemical Physics 67 (1977) 2246-2253.

[30] S. Sastry, P. G. Debenedetti, F. H. Stillinger, Nature 393 (1998) 554-557.

[31] F. H. Stillinger, Science 267 (1995) 1935-1939.

[32] V. Velikov, S. Borick, C. A. Angell, Journal of Physical Chemistry B 106 (2002) 1069-1080.

[33] C. A. Angell, S. Borick, Journal of Non-Crystalline Solids 307 (2002) 393-406.

[34] C. A. Angell, Journal of Non-Crystalline Solids 131 (1991) 13-31.

[35] R. J. Speedy, P. G. Debenedetti, Molecular Physics 88 (1996) 1293-1316.

[36] C. A. Angell, Journal of Research of the National Institute of Standards and Technology 102 (1997) 171-185.

[37] F. H. Stillinger, Journal of Chemical Physics 88 (1988) 7818-7825.

[38] P. G. Debenedetti, M. M. Atakan, R. J. Speedy, Journal of Chemical Physics 104 (1996) 5349-5350.

[39] C. A. Angell, K. J. Rao, Journal of Chemical Physics 57 (1972) 470.

[40] G. P. Johari, Journal of Chemical Physics 126 (2007) 114901.